

Current-driven spin oscillations in noncollinear antiferromagnetic tunnel junctions

Shanshan Hu ^{1,*}, Cuixiu Zheng ^{1,*}, Chao Chen ¹, Yan Zhou ^{2,†} and Yaowen Liu ^{1,3,‡}

¹*School of Physics Science and Engineering, Tongji University, Shanghai 200092, People's Republic of China*

²*School of Science and Engineering, The Chinese University of Hong Kong, Shenzhen 518172, People's Republic of China*

³*Shanghai Key Laboratory for Special Artificial Microstructure Materials and Technology, Tongji University, Shanghai 200092, People's Republic of China*



(Received 15 November 2023; revised 11 March 2024; accepted 25 April 2024; published 20 May 2024)

This study investigates the fascinating reality of noncollinear antiferromagnet Mn_3Pt thin film and its potential applications in spintronic devices, particularly in the context of all-antiferromagnetic tunnel junctions. By employing atomic-scale Landau-Lifshitz-Gilbert (LLG) simulations, we explored the spin dynamics driven by spin transfer torque (STT) in a Mn_3Pt -based all-antiferromagnetic tunnel junction. The investigation revealed an intriguing phenomenon: a spin-flop transition occurring within the Mn_3Pt sublattices under the influence of STT. This transition involves a transformation from a triangular antiparallel alignment to a quasiparallel configuration, demonstrating the complex dynamics achievable through STT manipulation. Importantly, the study identifies magnetic anisotropy as a key determinant of the stability of the spin-flop process, highlighting that larger magnetic anisotropy leads to a more robust transition. Furthermore, through frequency analyses conducted via simulations and theoretical considerations, the study elucidates the presence of terahertz oscillations. Notably, the frequency of these oscillations exhibits a linear increase with the increase of current density. These findings not only deepen our understanding of the oscillation properties of noncollinear antiferromagnets but also pave the way for potential applications in high-frequency spin oscillators.

DOI: [10.1103/PhysRevB.109.174433](https://doi.org/10.1103/PhysRevB.109.174433)

I. INTRODUCTION

Antiferromagnets (AFMs) constitute a class of materials characterized by an antiferromagnetic arrangement of spins, resulting in a net magnetic moment of zero. They hold significant promise for advancing next-generation spintronic technology [1–4], owing to their inherently low stray magnetic fields, which enable high storage density [5]. Moreover, the strong direct antiferromagnetic exchange interactions endow AFMs with remarkable stability against external magnetic interference and facilitate ultrafast terahertz (THz) spin wave dynamics, suggesting their potential as high-frequency THz sources [6–8]. While extensively studied collinear antiferromagnets such as MnF_2 and Mn_2Au [9–11] can be described by the Néel vector $l = \mathbf{m}_1 - \mathbf{m}_2$ and net magnetization $\mathbf{m} = \mathbf{m}_1 + \mathbf{m}_2$, where \mathbf{m}_1 and \mathbf{m}_2 represent the magnetic moments of the constituent atoms [12,13], recent focus has shifted towards noncollinear AFMs. In noncollinear AFMs such as Mn_3X ($X = \text{Sn, Ge, Ir, or Pt}$) and antiperovskites Mn_3AN ($A = \text{Ga, Sn, or Ni}$), the fundamental unit consists of at least three sublattices. These noncollinear AFMs exhibit unique spin configurations and possess nonzero Berry curvature, leading to a wide range of novel magnetic properties, including the spin Hall effect [14,15], anomalous

Hall effect [16–18], anomalous Nernst effect [19,20], and magneto-optical Kerr effect [21].

Noncollinear AFMs offer remarkable versatility in various aspects, including electrical controllability as a free layer in spintronic devices [22–27] and the generation of spin-polarized currents [28–32]. These characteristics, coupled with their vanishing stray fields and capacity for ultrafast spin dynamics, make them particularly attractive for applications [33–35]. Recent experimental advancements, such as the all-antiferromagnetic tunnel junction (AATJ) [36,37] that consists of noncollinear AFM/MgO/noncollinear AFM layers, demonstrate tunneling magnetoresistance (TMR) at room temperature, highlighting the potential for utilizing noncollinear AFMs in efficient spintronic devices and novel concepts.

This paper conducts atomic-scale dynamical simulations to investigate spin oscillations in the noncollinear AFM Mn_3Pt under a dc current, employing an AATJ structure composed of $\text{MnPt}/\text{Mn}_3\text{Pt}/\text{MgO}/\text{Mn}_3\text{Pt}$ [36] [depicted in Fig. 1(a)]. The simulations unveil alterations in the precession orbits represented by the magnetizations of the three Mn_3Pt sublattices and analyze system energy during the steady-state oscillations. Notably, antiferromagnetic exchange couplings can induce a spin-flop state within noncollinear AFMs when the spin transfer torque (STT) reaches a certain threshold, albeit weak magnetic anisotropy can destabilize this state. The oscillation frequency of the order parameter can be tuned to the THz range. These atomic-scale models contribute significantly to antiferromagnetic spintronic devices, particularly regarding current-induced auto-oscillatory behaviors,

*These authors contributed equally to this work.

†Corresponding author: zhouyan@cuhk.edu.cn

‡Corresponding author: yaowen@tongji.edu.cn

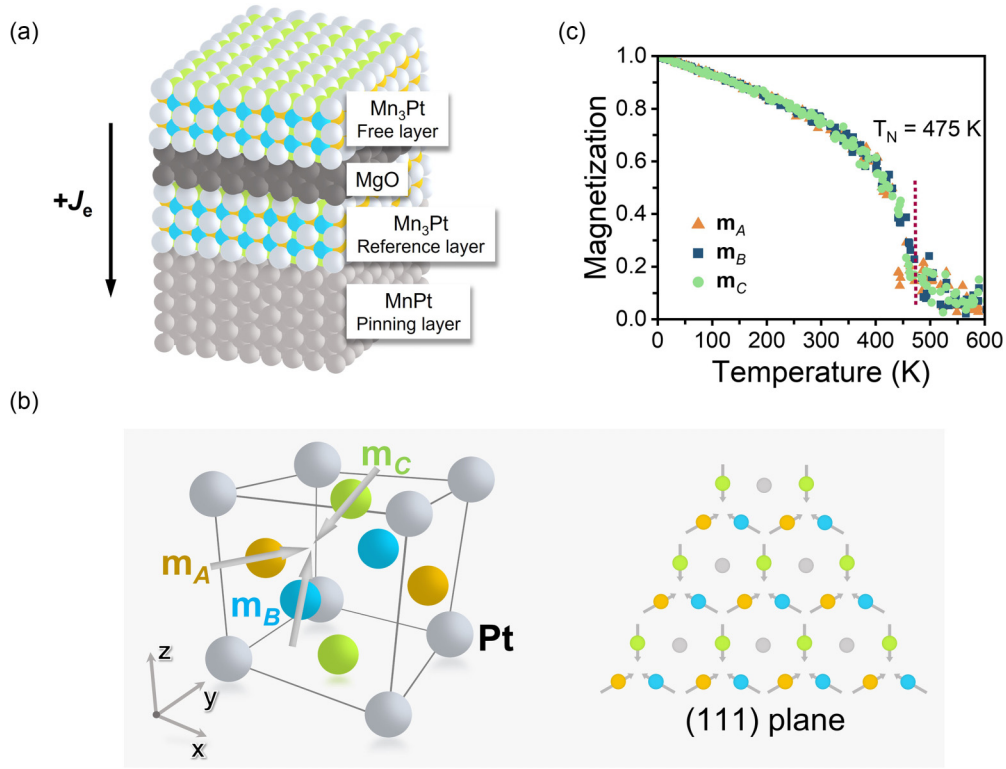


FIG. 1. (a) Schematic representation of an AATJ consisting of MnPt/Mn₃Pt/MgO/Mn₃Pt. The direction of positive current is indicated, flowing the free layer to the reference layer. (b) Crystal and magnetic structure of Mn₃Pt, with gray balls representing Pt atoms and colored balls with arrows indicating Mn atoms of three sublattices. The colors yellow, blue, and green represent \mathbf{m}_A , \mathbf{m}_B , and \mathbf{m}_C , respectively. The hexagonal spin structure of Mn₃Pt in the (111) kagome plane, where Mn atoms are at the corners of each hexagon while the Pt atoms are at the center (gray). The spins on neighboring Mn atoms are aligned at an angle of $\sim 120^\circ$ with respect to each other. (c) Simulated magnetization plotted against temperature for the three Mn sublattices, from which the Néel temperature (~ 475 K) is determined.

and offer insights into the dynamics of noncollinear AFM applications in electrical current-driven spintronic devices and THz signal sources.

II. METHOD

In our simulations, we employed the VAMPIRE software package [38] to investigate atomic spin dynamics. The Mn₃Pt alloy films were modeled using three groups of sublattices with triangular opposite alignment, characteristic of antiferromagnetic coupling. The localized energy of the Mn₃Pt system was described by a spin Hamiltonian incorporating both exchange energy and anisotropy energy:

$$E = - \sum_{i < j} J_{ij} \mathbf{m}_i \cdot \mathbf{m}_j - \frac{K}{2} \sum (\mathbf{m}_i \cdot \mathbf{e}_{ik})^2, \quad (1)$$

where \mathbf{m}_i and \mathbf{m}_j represent the spin directions of the i th Mn atom and its j th neighbor atom, respectively. J_{ij} denotes the isotropic exchange coupling between magnetic sublattices, with values of $J_{ij}^N = -4.192 \times 10^{-21}$ J/link for the nearest antiferromagnetic exchange coupling and $J_{ij}^{NN} = 2.15 \times 10^{-21}$ J/link for effective next-nearest exchange interactions (ferromagnetic exchange coupling). $K = -1 \times 10^{-25}$ J/atom represents the Néel pair anisotropy constant [36,39], and \mathbf{e}_{ik}

is a unit vector connecting the i th Mn site with its k th nearest-neighbor Pt atoms. The minimization of Néel anisotropy energy leads to noncollinear antiferromagnetic textures in Mn₃Pt.

Here we consider an AATJ sample with a structure similar to experiments [36]: substrate MnPt/Mn₃Pt/MgO/Mn₃Pt, as illustrated in Fig. 1(a). The bottom AFM reference layer, noncollinear Mn₃Pt, is exchange biased by a collinear AFM MnPt layer. The top noncollinear Mn₃Pt layer serves as the free layer, with dimensions of $5 \times 5 \times 2$ nm and the (111) plane of its fcc crystal phase identified as the kagome plane [see Fig. 1(b)]. The unit cell contains three magnetic Mn atoms and a nonmagnetic Pt atom. The magnetic atoms are represented by the sublattices of $\mathbf{m}_\zeta = (m_{\zeta x}, m_{\zeta y}, m_{\zeta z})$ [40] with the z axis along the [001] direction (where $\zeta = A, B, C$). The reference layer is also (001)-oriented Mn₃Pt whose direction is fixed by a MnPt pinning layer. The spin polarization direction of the reference layer is aligned with a magnetic field applied along the [001] direction [36]. Owing to momentum-dependent spin polarization originating in the broken symmetries of Mn₃Pt, the application of a weak magnetic field (typically in a few mT) is feasible to flip the noncollinear spin configurations for generating the z -direction projection of spin expectation [36,41]. In contrast, the applied magnetic field is not enough to change the magnetic state of the Mn₃Pt reference layer due

to the strong antiferromagnetic coupling from the MnPt pinning layer. Therefore, the Zeeman energy that originated from magnetic fields was not considered in the spin Hamiltonian of Eq. (1).

A zero-field cooling process from 1000 to 0 K returned the system to a ground state of the Mn₃Pt free layer with spins arranged in a head-to-head or tail-to-tail configuration on the (111) crystal plane, corresponding to the ordered $L1_2$ phase with $Pm\bar{3}m$ space group. This configuration, characterized by the 120° angles between adjacent spins [as shown in Fig. 1(b)], is consistent with previous studies [42,43]. Additionally, the temperature-dependent sublattice magnetization curves obtained from the same simulation match well with recent research findings, with the Néel temperature of around 475 K [17,44], as shown in Fig. 1(c).

Spin dynamics simulations at atomic level are conducted by using the Landau-Lifshitz-Gilbert (LLG) equation, given by Eq. (2) [38,45]:

$$\frac{\partial \mathbf{m}_i}{\partial t} = -\frac{\gamma}{(1+\lambda^2)} [\mathbf{m}_i \times \mathbf{H}_{\text{eff}}^i + \lambda \mathbf{m}_i \times (\mathbf{m}_i \times \mathbf{H}_{\text{eff}}^i)]. \quad (2)$$

Here, $\gamma = 1.76 \times 10^{11} \text{ s}^{-1} \text{ T}^{-1}$ is the gyromagnetic ratio, and $\lambda = 0.01$ is the Gilbert-damping constant. The effective field on the i th sublattices, $\mathbf{H}_{\text{eff}}^i = -\mu_s^{-1} \partial E / \partial \mathbf{m}_i + \mathbf{H}_{\text{th}}^i$, is derived from the spin Hamiltonian, where $\mathbf{H}_{\text{th}}^i = \Gamma(t) \sqrt{2\lambda k_B T / \gamma \mu_s \Delta t}$ is the thermal field described by a Gaussian distribution [46]. In order to eliminate the contribution of thermal perturbations, all dynamical simulations are conducted at $T = 0$ K. The current-induced STT effect is described as an effective field formula, given by [47]

$$\mathbf{H}_{\text{STT}}^i = a_{j_e} (\mathbf{m}_i \times \mathbf{p}) + b_{j_e} \mathbf{p}. \quad (3)$$

This equation accounts for both dampinglike (a_{j_e}) and fieldlike (b_{j_e}) components of the STT effective field in tesla. The spin polarization \mathbf{p} of this study is assumed to be in the $-z$ direction. As mentioned above, the atomic-scale calculations based on the discrete energy model require more precise effective field expressions to avoid the effects of temperature-dependent saturation magnetization and the thickness definition. The expressions of a_{j_e} and b_{j_e} for a single sublattice in a unit cell are given by [48,49]

$$a_{j_e} = \frac{\hbar \eta J_e a^2}{2|e|(1+\chi \mathbf{m}_i \cdot \mathbf{p}) \mu_s}$$

$$b_{j_e} = \beta \frac{\hbar \eta J_e a^2}{2|e|(1+\chi \mathbf{m}_i \cdot \mathbf{p}) \mu_s} = \beta a_{j_e}, \quad (4)$$

where \hbar is the reduced Planck constant, J_e is the current density with units in A/m^2 , $\eta = 0.085$ is the STT efficiency [29], $|e| = 1.602 \times 10^{-19} \text{ C}$ is the electric charge, $\mu_s = 3.0 \mu_B$ is the local spin moment, and $a = 3.833 \text{ \AA}$ is the unit cell length [42,44]. The spin-torque asymmetry χ is taken as $\chi = 0$ for simplification, and β is the ratio of the fieldlike equivalent field compared to the dampinglike equivalent field, which is also considered as zero for simplification. Therefore, the STT equivalent field H_{STT} mentioned in the following content is equivalent to a_{j_e} .

III. RESULTS AND DISCUSSION

As stable magnetization oscillations are excited, the evolution of spin configurations with respect to current strength can be categorized into three distinct intervals, as illustrated in Fig. 2.

The first state is the *triangular antiparallel state*. In this state, the three Mn sublattices within a unit cell maintain a head-to-head or tail-to-tail configuration. Despite the increase in the STT equivalent field, \mathbf{m}_C remains immobile, experiencing a pull toward the $-z$ axis due to its proximity to the polarization direction. Meanwhile, the out-of-plane polarization drives oscillations in the x and y components of \mathbf{m}_A and \mathbf{m}_B , leading them to stabilize on the same precession trajectory, as depicted in Fig. 2(a). Notably, \mathbf{m}_A and \mathbf{m}_B share a common orbit ($m_{Az} = m_{Bz}$) in this state, with their oscillations exhibiting a phase displacement of π .

The second state is the *unstable spin-flop state*. With a further increase in the STT field, the spin configurations enter an unstable state due to the competition between STT and antiferromagnetic coupling. This behavior resembles the spin-flop state commonly observed in collinear AFMs. In this state, at least two sublattices tilt toward the $-z$ axis, and each sublattice occupies a separate orbit. A typical configuration of this state is depicted in Fig. 2(b).

The third state is referred to as the *quasiparallel state*, depicted in Fig. 2(c). It occurs when the injection current becomes strong enough to overcome the antiferromagnetic coupling interaction. Here, all sublattices incline toward the $-z$ axis due to the orientation of the fixed layer's polarization direction. Accordingly, the x and y components of all sublattice magnetizations precess stably around the z axis and gradually converge onto a common z -axis trajectory. This results in oscillations with a phase displacement of $2\pi/3$ between any two of them until they all align completely parallel to the $-z$ axis.

In order to elucidate the role of the STT effect on the Mn₃Pt free layer, we summarize the evolution of the z components of \mathbf{m}_A , \mathbf{m}_B , and \mathbf{m}_C in response to the effective STT fields (currents), as depicted in Fig. 3. The simulation results, derived from the aforementioned material parameters of Mn₃Pt, are illustrated in Figs. 3(c) and 3(d). In Fig. 3(c), the yellow region represents the triangular antiparallel state, the white region corresponds to the unstable spin-flop state, and the blue region represents the quasiparallel state. These states are determined by the magnitude of the STT equivalent field (current). The metastable region spans approximately 1.27 T, as indicated by the gray region in Fig. 3(d). Figure 2 indicates that the in-plane components of net magnetization ($m_{Ax} + m_{Bx} + m_{Cx}$ and $m_{Ay} + m_{By} + m_{Cy}$) are zero, with this outcome being attributed to the out-of-plane spin polarization in the reference layer and the absence of external disturbances in the xy plane. As a result, the in-plane net magnetization remains unaffected and stays at zero. This implies that the net magnetization of the free-layer Mn₃Pt can be characterized solely by its m_z component. Furthermore, it suggests that the m_z component linearly increases as a function of the STT equivalent field.

In collinear AFMs, the application of external influences such as an external field \mathbf{H} along the anisotropy axes triggers a spin-flop transition. For $H < H_{\text{sf}}$ (spin-flop field), two

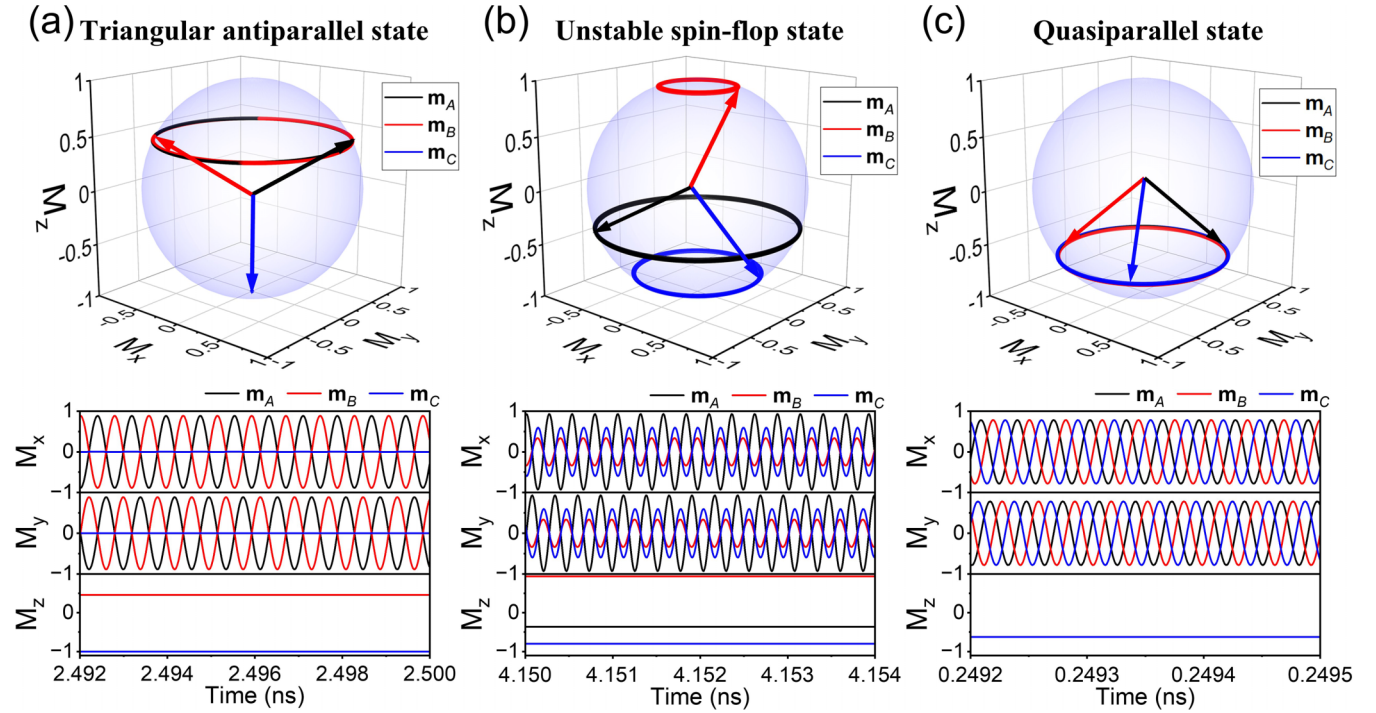


FIG. 2. Current-driven magnetization precession of the Mn₃Pt free layer, showcasing three distinct precession states as a function of the current (J_e): (a) triangular antiparallel state, $J_e = 3 \times 10^{12}$ A/m²; (b) unstable spin-flop state, $J_e = 9 \times 10^{12}$ A/m²; and (c) quasiparallel state, $J_e = 8 \times 10^{13}$ A/m².

sublattices \mathbf{m}_A and \mathbf{m}_B maintain an antiparallel configuration, resulting in $|\mathbf{m}| = |\mathbf{m}_A + \mathbf{m}_B| = 0$. For $H > H_{sf}$, both \mathbf{m}_A and \mathbf{m}_B orient toward the direction of \mathbf{H} , and $|\mathbf{m}|$ reaches a certain constant value, increasing linearly with the augmentation of H [50]. However, in the case of Mn₃Pt, when m_{Cz} is excluded, the three-body problem can be transformed into a two-body problem, resulting in a discontinuous change in the net magnetization when the STT equivalent field exceeds a certain threshold. This discontinuity is shown by the orange squares and solid line in Fig. 3(d).

Magnetic anisotropy stands as a crucial property, subject to empirical tuning through strain or pressure application [26,51,52]. Therefore, we investigate the impact of anisotropy by adjusting the Néel pair anisotropy constant in our simulations. In Fig. 3(a), the Néel pair anisotropy is set to

$K = -1 \times 10^{-24}$ J/atom. The metastable region, where different states can coexist, diminishes. Furthermore, the variations in m_{Az} , m_{Bz} , and m_{Cz} with the STT field become more akin to those observed in collinear AFMs. Figure 3(e) shows the corresponding evolution of m_z with $K = -1 \times 10^{-26}$ J/atom. The reduction in magnetic anisotropy enlarges the width of the metastable region to approximately 1.44 T. Despite the marked disparities in magnetic anisotropies, the progression of m_z with the STT equivalent field endures a linear trajectory, as depicted in Figs. 3(b) and 3(f). Consequently, m_z evolutions remain unaffected by the influence of magnetic anisotropy.

To gain further insight into the mechanism of the current-induced magnetization precession theoretically, we begin with an energy perspective by considering the free-energy density of the three-body systems, defined as

$$\begin{aligned}
 E_{\text{tot}} &= E_{\text{exchange}} + E_{\text{anisotropy}} \\
 E_{\text{exchange}} &= -\frac{1}{2} \left[8J_{ij}^{\text{N}} (m_{A,i} \cdot m_{B,j} + m_{A,i} \cdot m_{C,j} + m_{B,i} \cdot m_{C,j}) + 6J_{ij}^{\text{NN}} (m_{A,i} \cdot m_{A,j} + m_{B,i} \cdot m_{B,j} + m_{C,i} \cdot m_{C,j}) \right] \\
 E_{\text{anisotropy}} &= -\frac{K}{2} \sum_{\zeta=A,B,C} \sum_{k=1}^4 (\mathbf{m}_{\zeta} \cdot \mathbf{e}_{\zeta k})^2,
 \end{aligned} \tag{5}$$

where i and j are only used to distinguish one Mn sublattice from their neighbor site Mn sublattices. Each Mn sublattice (\mathbf{m}_A , \mathbf{m}_B , or \mathbf{m}_C) has eight nearest-neighbor exchange interactions and six next-nearest-neighbor exchange interactions. The introduction of a silent factor of 1/2 in the exchange

energy of Eq. (5) comes from a redundancy of calculation to avoid double-counting of the exchange interactions. For the anisotropy energy calculation, $\mathbf{e}_{\zeta k}$ denotes the direction of the easy axis connecting the \mathbf{m}_{ζ} sublattice with its k th nearest-neighbor Pt atoms (each Mn atom has four nearest-neighbor

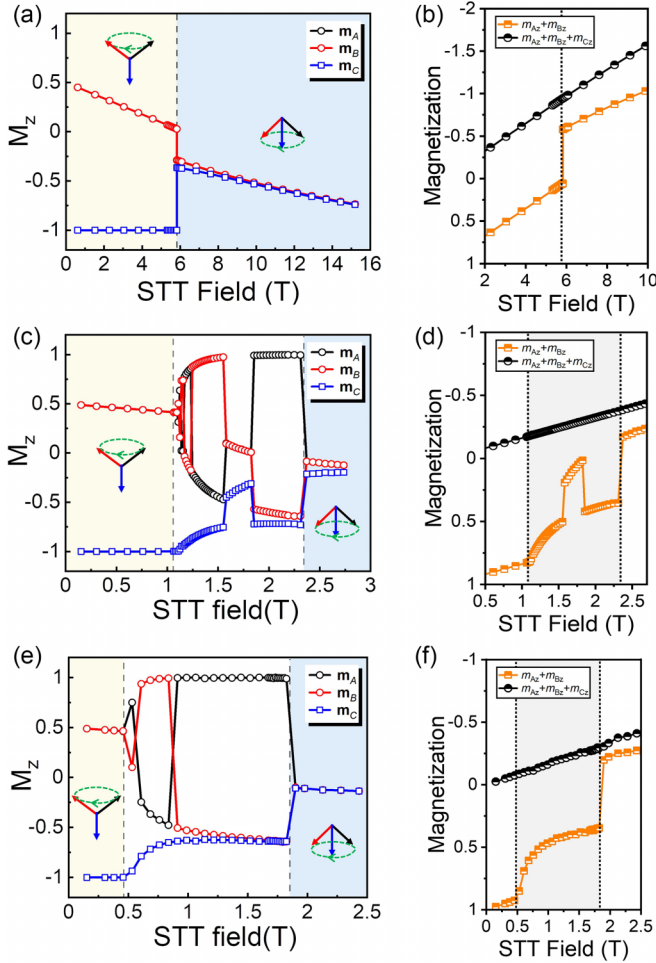


FIG. 3. Evolution of the z component of individual sublattice magnetization in the stable oscillation state of the free-layer Mn_3Pt : (a) $K = -1 \times 10^{-24}$ J/atom; (c) $K = -1 \times 10^{-25}$ J/atom; and (e) $K = -1 \times 10^{-26}$ J/atom versus STT equivalent fields. Black, red, and blue arrows denote the magnetization direction of \mathbf{m}_A , \mathbf{m}_B , and \mathbf{m}_C , respectively. (b), (d), and (f) show the corresponding discrepancies in trends between the net magnetization $m_{Az} + m_{Bz} + m_{Cz}$ and $m_{Az} + m_{Bz}$.

Pt atoms). Consequently, each sublattice is associated with four $\mathbf{e}_{\zeta k}$. For example, the directions of the easy axes \mathbf{e}_{A_k} for \mathbf{m}_A can be written in detail as $(0, 1, 1)$, $(0, -1, 1)$, $(0, 1, -1)$, and $(0, -1, -1)$. By substituting $m_{\zeta x}^2 + m_{\zeta y}^2 + m_{\zeta z}^2 = 1$, $m_{Ax} + m_{Bx} + m_{Cx} = 0$, and $m_{Ay} + m_{By} + m_{Cy} = 0$, we can simplify Eq. (5) into

$$E_{\text{tot}} = -2J_{ij}^N m_z^2 + 6J_{ij}^N - 9J_{ij}^{NN} - 2K[3 - (m_{Ax}^2 + m_{By}^2 + m_{Cz}^2)], \quad (6)$$

where m_z is the net magnetization of the free-layer Mn_3Pt . To examine the effect of various interactions on the system, the energy analysis is conducted for $K = -1 \times 10^{-25}$ J/atom as a function of m_z , as shown in Fig. 4. Notably, under a consistent STT equivalent field, the total energy E_{tot} and exchange energy E_{exchange} are nearly equal, suggesting a minimal energy contribution from magnetic anisotropy. Thus, we can

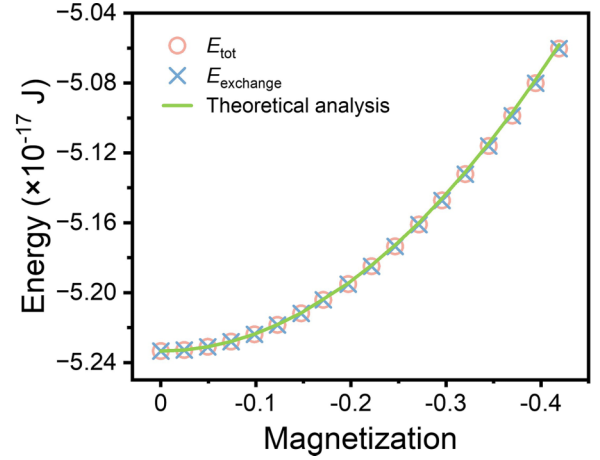


FIG. 4. The net magnetization dependence of total energy E_{tot} (circles) and exchange energy E_{exc} (crosses). The green line is obtained from Eq. (6) with Eq. (11).

temporarily assume $E_{\text{tot}} \approx E_{\text{exchange}} = -2J_{ij}^N m_z^2 + 6J_{ij}^N - 9J_{ij}^{NN}$ in the next calculation.

Next, to facilitate the analysis of magnetization precession, we introduce an angular velocity $\omega_{\zeta p}$ ($\zeta = A, B, C$) around the polarization direction (z axis) to describe the precession angular velocity of the sublattices. We simplify Eq. (2) to the standard LLG equation and consider STT as an independent term. For simplicity, we consider only a single sublattice in the following derivation. The LLG equation in the laboratory coordinate system is written as

$$\left[\frac{d\mathbf{m}_{\zeta}}{dt} \right]_L = -\gamma \left(\frac{\nabla_{\mathbf{m}_{\zeta}} E_{\zeta \text{tot}}}{\mu_s} \right) \times \mathbf{m}_{\zeta} + \lambda \mathbf{m}_{\zeta} \times \left[\frac{d\mathbf{m}_{\zeta}}{dt} \right]_L + \gamma H_{\text{STT}} \mathbf{m}_{\zeta} \times (\mathbf{m}_{\zeta} \times \mathbf{p}). \quad (7)$$

It is possible to utilize the rotation (R) frame around the z axis in relation to the inertia laboratory (L) frame through a coordinate transform [53,54]: $[d\mathbf{m}_{\zeta}/dt]_R = [d\mathbf{m}_{\zeta}/dt]_L - \omega_{\zeta p} \mathbf{p} \times \mathbf{m}_{\zeta}$. Thus, Eq. (7) can be rewritten as the following equation in the rotation frame [55–58]:

$$\left[\frac{d\mathbf{m}_{\zeta}}{dt} \right]_R = -\gamma \left(\frac{\nabla_{\mathbf{m}_{\zeta}} E_{\zeta \text{tot}}}{\mu_s} + \frac{\omega_{\zeta p}}{\gamma} \mathbf{p} \right) \times \mathbf{m}_{\zeta} + \lambda \mathbf{m}_{\zeta} \times \left[\frac{d\mathbf{m}_{\zeta}}{dt} \right]_R + (\gamma H_{\text{STT}} - \lambda \omega_{\zeta p}) \mathbf{m}_{\zeta} \times (\mathbf{m}_{\zeta} \times \mathbf{p}). \quad (8)$$

For a stable magnetization precession around the z axis, the damping torque should be counterbalanced by the driving source of STT, leading to $\gamma H_{\text{STT}} = \lambda \omega_{\zeta p}$. In this case, the third term of Eq. (8) is eliminated in the rotation frame, and Eq. (8) can be rewritten as

$$\left[\frac{d\mathbf{m}_{\zeta}}{dt} \right]_R = -\gamma \left(\frac{\nabla_{\mathbf{m}_{\zeta}} E_{\zeta \text{rot}}}{\mu_s} \right) \times \mathbf{m}_{\zeta} + \lambda \mathbf{m}_{\zeta} \times \left[\frac{d\mathbf{m}_{\zeta}}{dt} \right]_R, \quad (9)$$

where E_{rot} contains the energy in the laboratory coordinate system and the equivalent energy of STT $E_{\zeta \text{STT}} = \mu_s \int (\omega_{\zeta p} / \gamma) d\mathbf{m}_{\zeta z} = \mu_s \int (H_{\text{STT}} / \lambda) d\mathbf{m}_{\zeta z} = (\mu_s H_{\text{STT}} / \lambda) m_{\zeta z}$. We integrate the three sublattices into one system, thus the total

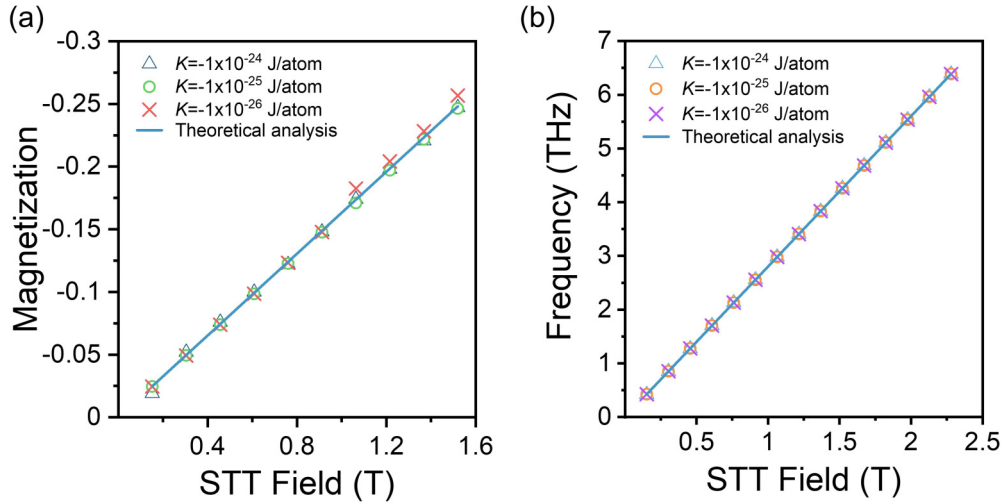


FIG. 5. The dependence of (a) net magnetization and (b) oscillation frequency on the STT equivalent fields at various anisotropies. The solid lines are the theoretical results calculated from Eq. (11) for plot (a) and from Eq. (12) for plot (b).

equivalent energy of the system reads

$$E_{\text{rot}} \approx E_{\text{tot}} + E_{\text{STT}} = -2J_{ij}^N m_z^2 + 6J_{ij}^N - 9J_{ij}^{NN} + \frac{\mu_s H_{\text{STT}}}{\lambda} m_z. \quad (10)$$

It should be noted that when the magnetic moment direction of one sublattice aligns with the polarization direction \mathbf{p} (either parallel or antiparallel), such as \mathbf{m}_C in the triangular antiparallel state depicted in Fig. 2(a), $\omega_{CP} = 0$, and the change of E_{rot} is mainly governed by \mathbf{m}_A and \mathbf{m}_B . The equilibrium state corresponds to the minimum of Eq. (10) with respect to m_z . Therefore, by evaluating $\partial E_{\text{rot}} / \partial m_z = 0$, one can obtain the m_z dependence as

$$m_z = \frac{\mu_s}{4\lambda J_{ij}^N} H_{\text{STT}} \quad (\text{when } \gamma H_{\text{STT}} = \lambda \omega_{CP}). \quad (11)$$

Equation (11) clearly demonstrates the relationship between the m_z and both the STT equivalent field and the antiferromagnetic exchange constant. For a certain value of J_{ij}^N , the m_z is linearly proportional to the STT equivalent field. This analytical result is in good agreement with the simulation results shown in Fig. 5(a). By substituting the analyzed m_z into E_{tot} , as illustrated in Fig. 4, we analytically obtain the system energy represented by the green line, which is in good agreement with the simulation results. Additionally, the exchange interactions can affect the m_z value of systems for a given STT, but the extent of the magnetic anisotropy still plays a significant role in determining the m_z of individual Mn atoms.

Finally, the relationship between the frequency and the STT equivalent field is derived as

$$f = \frac{\omega_{CP}}{2\pi} = \frac{\gamma H_{\text{STT}}}{2\pi\lambda}. \quad (12)$$

This analytical result agrees well with the simulation results of the frequency of \mathbf{m}_B as a function of the STT equivalent field presented in Fig. 5(b), confirming that f increases almost linearly with H_{STT} [24,59,60]. Leaving aside any assumptions about balancing oscillations, the frequency is indeed related to the effective field. In our system, the effective field can be approximated as the exchange field, represented by $H_{\text{eff}} = 4J_{ij}^N m_z / \mu_s$. Consequently, f is, in fact, a function

of m_z . The consistent trend observed between Fig. 5(a) and 5(b) precisely indicates this relationship.

IV. CONCLUSION

In conclusion, we have developed an atomic-scale simulation model for all-antiferromagnetic tunnel junctions, employing the noncollinear AFM Mn_3Pt as the free layer. The presence of the unique magnetic symmetry of noncollinear AFMs facilitates the generation of out-of-plane spin polarization. This setup enables stable spin oscillations in the free-layer Mn_3Pt , driven by STT, and exhibiting terahertz frequencies. Three distinct oscillation states are identified with varying STT strength: the triangular antiparallel state, the unstable spin-flop state, and the quasiparallel state. The presence of an unstable region, influenced by magnetic anisotropy, precedes the deterministic flip in Mn_3Pt . Exchange interactions primarily affect the net magnetization under given STT equivalent fields. Moreover, the oscillation frequency of Mn_3Pt sublattices shows a linear relationship with STT equivalent fields, falling within the THz range. This study provides a comprehensive understanding of spin dynamics in noncollinear AFMs and offers insights into the potential mechanism of magnetization dynamics in spin-torque oscillators based on noncollinear antiferromagnetic tunnel junctions. However, in order to improve the performance of antiferromagnetic tunnel junctions, further investigations are required to quantify the strength of the magnetic field, charge current, and resulting spin current injected into the noncollinear antiferromagnetic free layer, as well as the current-induced magnetic switching and oscillations.

ACKNOWLEDGMENTS

Y.L. and C.Z. acknowledge support from National Natural Science Foundation of China (NSFC) (Grants No. 51971161, No. 12274322, and No. 12347174). Y.Z. acknowledges support by the Shenzhen Fundamental Research Fund (Grant No. JCYJ20210324120213037), the Guangdong Basic and Applied Basic Research Foundation

(2021B1515120047), the Shenzhen Peacock Group Plan (KQTD20180413181702403), the National Natural Science

Foundation of China (12374123), and the 2023 SZSTI stable support scheme.

- [1] V. Baltz, A. Manchon, M. Tsoi, T. Moriyama, T. Ono, and Y. Tserkovnyak, Antiferromagnetic spintronics, *Rev. Mod. Phys.* **90**, 015005 (2018).
- [2] T. Jungwirth, X. Marti, P. Wadley, and J. Wunderlich, Antiferromagnetic spintronics, *Nat. Nanotechnol.* **11**, 231 (2016).
- [3] O. Gomonay, V. Baltz, A. Brataas, and Y. Tserkovnyak, Antiferromagnetic spin textures and dynamics, *Nat. Phys.* **14**, 213 (2018).
- [4] H. Bai, Y. C. Zhang, L. Han, Y. J. Zhou, F. Pan, and C. Song, Antiferromagnetism: An efficient and controllable spin source, *Appl. Phys. Rev.* **9**, 041316 (2022).
- [5] X. Marti, I. Fina, C. Frontera, J. Liu, P. Wadley, Q. He, R. J. Paull, J. D. Clarkson, J. Kudrnovský, I. Turek, J. Kuneš, D. Yi, J. H. Chu, C. T. Nelson, L. You, E. Arenholz, S. Salahuddin, J. Fontcuberta, T. Jungwirth, and R. Ramesh, Room-temperature antiferromagnetic memory resistor, *Nat. Mater.* **13**, 367 (2014).
- [6] R. Cheng, D. Xiao, and A. Brataas, Terahertz antiferromagnetic spin Hall nano-oscillator, *Phys. Rev. Lett.* **116**, 207603 (2016).
- [7] F. Keffer and C. Kittel, Theory of antiferromagnetic resonance, *Phys. Rev.* **85**, 329 (1952).
- [8] K. Olejník, T. Seifert, Z. Kašpar, V. Novák, P. Wadley, R. P. Campion, M. Baumgartner, P. Gambardella, P. Němec, J. Wunderlich, J. Sinova, P. Kužel, M. Müller, T. Kampfrath, and T. Jungwirth, Terahertz electrical writing speed in an antiferromagnetic memory, *Sci. Adv.* **4**, eaar3566 (2018).
- [9] S. Y. Bodnar, L. Šmejkal, I. Turek, T. Jungwirth, O. Gomonay, J. Sinova, A. A. Sapozhnik, H. J. Elmers, M. Kläui, and M. Jourdan, Writing and reading antiferromagnetic Mn_2Au by Néel spin-orbit torques and large anisotropic magnetoresistance, *Nat. Commun.* **9**, 348 (2018).
- [10] P. Vaidya, S. A. Morley, J. van Tol, Y. Liu, R. Cheng, A. Brataas, D. Lederman, and E. del Barco, Subterahertz spin pumping from an insulating antiferromagnet, *Science* **368**, 160 (2020).
- [11] S. M. Rezende, A. Azevedo, and R. L. Rodríguez-Suárez, Introduction to antiferromagnetic magnons, *J. Appl. Phys.* **126**, 151101 (2019).
- [12] H. V. Gomonay and V. M. Loktev, Spin transfer and current-induced switching in antiferromagnets, *Phys. Rev. B* **81**, 144427 (2010).
- [13] M. M. Bogdan and O. V. Charkina, Spin waves in easy-axis antiferromagnets with precessing domain walls, *Low Temp. Phys.* **40**, 84 (2014).
- [14] Y. Zhang, Y. Sun, H. Yang, J. Železný, S. P. P. Parkin, C. Felser, and B. Yan, Strong anisotropic anomalous Hall effect and spin Hall effect in the chiral antiferromagnetic compounds Mn_3X ($X = Ge, Sn, Ga, Ir, Rh, \text{ and } Pt$), *Phys. Rev. B* **95**, 075128 (2017).
- [15] Y. Zhang, J. Železný, Y. Sun, J. van den Brink, and B. Yan, Spin Hall effect emerging from a noncollinear magnetic lattice without spin-orbit coupling, *New J. Phys.* **20**, 073028 (2018).
- [16] H. Chen, Q. Niu, and A. H. MacDonald, Anomalous Hall effect arising from noncollinear antiferromagnetism, *Phys. Rev. Lett.* **112**, 017205 (2014).
- [17] Z. Q. Liu, H. Chen, J. M. Wang, J. H. Liu, K. Wang, Z. X. Feng, H. Yan, X. R. Wang, C. B. Jiang, J. M. D. Coey, and A. H. MacDonald, Electrical switching of the topological anomalous Hall effect in a non-collinear antiferromagnet above room temperature, *Nat. Electron.* **1**, 172 (2018).
- [18] S. Nakatsuji, N. Kiyohara, and T. Higo, Large anomalous Hall effect in a non-collinear antiferromagnet at room temperature, *Nature (London)* **527**, 212 (2015).
- [19] G.-Y. Guo and T.-C. Wang, Large anomalous Nernst and spin Nernst effects in the noncollinear antiferromagnets Mn_3X ($X = Sn, Ge, Ga$), *Phys. Rev. B* **96**, 224415 (2017).
- [20] X. Zhou, J.-P. Hanke, W. Feng, S. Blügel, Y. Mokrousov, and Y. Yao, Giant anomalous Nernst effect in noncollinear antiferromagnetic Mn-based antiperovskite nitrides, *Phys. Rev. Mater.* **4**, 024408 (2020).
- [21] T. Higo, H. Man, D. B. Gopman, L. Wu, T. Koretsune, O. M. J. van't Erve, Y. P. Kabanov, D. Rees, Y. Li, M. T. Suzuki, S. Patankar, M. Ikhlas, C. L. Chien, R. Arita, R. D. Shull, J. Orenstein, and S. Nakatsuji, Large magneto-optical Kerr effect and imaging of magnetic octupole domains in an antiferromagnetic metal, *Nat. Photonics* **12**, 73 (2018).
- [22] D. Y. Zhao, P. B. He, and M. Q. Cai, Terahertz oscillation in a noncollinear antiferromagnet under spin-orbit torques, *Phys. Rev. B* **104**, 214423 (2021).
- [23] T. Hajiri, S. Ishino, K. Matsuura, and H. Asano, Electrical current switching of the noncollinear antiferromagnet Mn_3GaN , *Appl. Phys. Lett.* **115**, 052403 (2019).
- [24] A. Shukla and S. Rakheja, Spin-torque-driven terahertz auto-oscillations in noncollinear coplanar antiferromagnets, *Phys. Rev. Appl.* **17**, 034037 (2022).
- [25] Y. Takeuchi, Y. Yamane, J. Y. Yoon, R. Itoh, B. Jinnai, S. Kanai, J. Ieda, S. Fukami, and H. Ohno, Chiral-spin rotation of non-collinear antiferromagnet by spin-orbit torque, *Nat. Mater.* **20**, 1364 (2021).
- [26] T. Higo, K. Kondou, T. Nomoto, M. Shiga, S. Sakamoto, X. Chen, D. Nishio-Hamane, R. Arita, Y. Otani, S. Miwa, and S. Nakatsuji, Perpendicular full switching of chiral antiferromagnetic order by current, *Nature (London)* **607**, 474 (2022).
- [27] A. Shukla, S. Qian, and S. Rakheja, Order parameter dynamics in Mn_3Sn driven by DC and pulsed spin-orbit torques, *APL Mater.* **11**, 091110 (2023).
- [28] J. Železný, Y. Zhang, C. Felser, and B. Yan, Spin-polarized current in noncollinear antiferromagnets, *Phys. Rev. Lett.* **119**, 187204 (2017).
- [29] H. Bai, X. F. Zhou, H. W. Zhang, W. W. Kong, L. Y. Liao, X. Y. Feng, X. Z. Chen, Y. F. You, Y. J. Zhou, L. Han, W. X. Zhu, F. Pan, X. L. Fan, and C. Song, Control of spin-orbit torques through magnetic symmetry in differently oriented noncollinear antiferromagnetic Mn_3Pt , *Phys. Rev. B* **104**, 104401 (2021).
- [30] T. Nan *et al.*, Controlling spin current polarization through non-collinear antiferromagnetism, *Nat. Commun.* **11**, 4671 (2020).
- [31] X. H. Wang, M. T. Hossain, T. R. Thapaliya, D. Khadka, S. Lendinez, H. Chen, M. F. Doty, M. B. Jungfleisch, S. X. Huang, X. Fan, and J. Q. Xiao, Spin currents with unusual spin

- orientations in noncollinear Weyl antiferromagnetic Mn_3Sn , *Phys. Rev. Mater.* **7**, 034404 (2023).
- [32] Y. You, H. Bai, X. Feng, X. Fan, L. Han, X. Zhou, Y. Zhou, R. Zhang, T. Chen, F. Pan, and C. Song, Cluster magnetic octupole induced out-of-plane spin polarization in antiperovskite antiferromagnet, *Nat. Commun.* **12**, 6524 (2021).
- [33] C. Song, R. Q. Zhang, L. Y. Liao, Y. Zhou, X. Zhou, R. Chen, Y. You, X. Chen, and F. Pan, Spin-orbit torques: Materials, mechanisms, performances, and potential applications, *Prog. Mater. Sci.* **118**, 100761 (2021).
- [34] H. Chen, P. Qin, H. Yan, Z. Feng, X. Zhou, X. Wang, Z. Meng, L. Liu, and Z. Liu, Noncollinear antiferromagnetic spintronics, *Mater. Lab* **1**, 220032 (2022).
- [35] O. R. Sulymenko, O. V. Prokopenko, V. S. Tiberkevich, A. N. Slavin, B. A. Ivanov, and R. S. Khymyn, Terahertz-frequency spin Hall auto-oscillator based on a canted antiferromagnet, *Phys. Rev. Appl.* **8**, 064007 (2017).
- [36] P. Qin, H. Yan, X. Wang, H. Chen, Z. Meng, J. Dong, M. Zhu, J. Cai, Z. Feng, X. Zhou, L. Liu, T. Zhang, Z. Zeng, J. Zhang, C. Jiang, and Z. Liu, Room-temperature magnetoresistance in an all-antiferromagnetic tunnel junction, *Nature (London)* **613**, 485 (2023).
- [37] X. Chen, T. Higo, K. Tanaka, T. Nomoto, H. Tsai, H. Idzuchi, M. Shiga, S. Sakamoto, R. Ando, H. Kosaki, T. Matsuo, D. Nishio-Hamane, R. Arita, S. Miwa, and S. Nakatsuji, Octupole-driven magnetoresistance in an antiferromagnetic tunnel junction, *Nature (London)* **613**, 490 (2023).
- [38] R. F. Evans, W. J. Fan, P. Chureemart, T. A. Ostler, M. O. Ellis, and R. W. Chantrell, Atomistic spin model simulations of magnetic nanomaterials, *J. Phys.: Condens. Matter* **26**, 103202 (2014).
- [39] S. Jenkins, R. W. Chantrell, and R. F. L. Evans, Atomistic simulations of the magnetic properties of $\text{Ir}_x\text{Mn}_{1-x}$ alloys, *Phys. Rev. Mater.* **5**, 034406 (2021).
- [40] Y. Yamane, O. Gomonay, and J. Sinova, Dynamics of non-collinear antiferromagnetic textures driven by spin current injection, *Phys. Rev. B* **100**, 054415 (2019).
- [41] L.-D. Yuan, Z. Wang, J.-W. Luo, and A. Zunger, Prediction of low-Z collinear and noncollinear antiferromagnetic compounds having momentum-dependent spin splitting even without spin-orbit coupling, *Phys. Rev. Mater.* **5**, 014409 (2021).
- [42] Y. Kota, H. Tsuchiura, and A. Sakuma, Ab-initio study on the magnetic structures in the ordered Mn_3Pt alloy, *IEEE Trans. Magn.* **44**, 3131 (2008).
- [43] G. Li, Q. Yang, K. Manna, C. Fu, H. Deniz, J. Jena, F. Li, S. Parkin, G. Auffermann, Y. Sun, and C. Felser, Optimization of catalytic active sites in non-collinear antiferromagnetic Mn_3Pt bulk single-crystal, *Mater. Today Phys.* **10**, 100137 (2019).
- [44] E. Krén, G. Kádár, L. Pál, J. Sólyom, P. Szabó, and T. Tarnóczy, Magnetic structures and exchange interactions in the Mn-Pt system, *Phys. Rev.* **171**, 574 (1968).
- [45] M. O. A. Ellis, R. F. L. Evans, T. A. Ostler, J. Barker, U. Atxitia, O. Chubykalo-Fesenko, and R. W. Chantrell, The Landau-Lifshitz equation in atomistic models, *Low Temp. Phys.* **41**, 705 (2015).
- [46] R. F. L. Evans, U. Atxitia, and R. W. Chantrell, Quantitative simulation of temperature-dependent magnetization dynamics and equilibrium properties of elemental ferromagnets, *Phys. Rev. B* **91**, 144425 (2015).
- [47] S. Zhang, P. M. Levy, and A. Fert, Mechanisms of spin-polarized current-driven magnetization switching, *Phys. Rev. Lett.* **88**, 236601 (2002).
- [48] A. Meo, S. Sampan-a-pai, P. B. Visscher, R. Chepulskyy, D. Apalkov, J. Chureemart, P. Chureemart, R. W. Chantrell, and R. F. L. Evans, Spin transfer torque switching dynamics in CoFeB/MgO magnetic tunnel junctions, *Phys. Rev. B* **103**, 054426 (2021).
- [49] J. C. Slonczewski, Currents, torques, and polarization factors in magnetic tunnel junctions, *Phys. Rev. B* **71**, 024411 (2005).
- [50] O. Prokhnenko, G. Marmorini, S. E. Nikitin, D. Yamamoto, A. Gazizulina, M. Bartkowiak, A. N. Ponomaryov, S. A. Zvyagin, H. Nojiri, I. F. Díaz-Ortega, L. M. Anovitz, A. I. Kolesnikov, and A. Podlesnyak, High-field spin-flop state in green diopside, *Phys. Rev. B* **103**, 014427 (2021).
- [51] M. Ikhlas, S. Dasgupta, F. Theuss, T. Higo, S. Kittaka, B. J. Ramshaw, O. Tchernyshyov, C. W. Hicks, and S. Nakatsuji, Piezomagnetic switching of the anomalous Hall effect in an antiferromagnet at room temperature, *Nat. Phys.* **18**, 1086 (2022).
- [52] P. A. Quintero, D. Rajan, M. K. Peprah, T. V. Brinzari, R. S. Fishman, D. R. Talham, and M. W. Meisel, Pressure-induced enhancement of the magnetic anisotropy in $\text{Mn}(\text{N}(\text{CN})_2)_2$, *Phys. Rev. B* **91**, 014439 (2015).
- [53] X. Zhang, H.-H. Chen, Z. Zhang, and Y. Liu, Electric-field assisted spin torque nano-oscillator and binary frequency shift keying modulation, *J. Magn. Magn. Mater.* **452**, 458 (2018).
- [54] Y. Wang, C. Zheng, D. Zhang, H.-H. Chen, and Y. Liu, Binary frequency shift keying modulation in spin torque oscillators with synthetic antiferromagnetic layer, *Appl. Phys. Lett.* **123**, 122406 (2023).
- [55] J. C. Slonczewski, Current-driven excitation of magnetic multilayers, *J. Magn. Magn. Mater.* **159**, L1 (1996).
- [56] T. Taniguchi, D. Saida, Y. Nakatani, and H. Kubota, Magnetization switching by current and microwaves, *Phys. Rev. B* **93**, 014430 (2016).
- [57] H. Chen, L. Zeng, C. Lee, and W. Zhao, Stability analysis of spin-torque nano-oscillator in the rotating frame, *Spin* **09**, 1950008 (2019).
- [58] H.-H. Chen, C.-M. Lee, L. Zeng, W.-S. Zhao, and C.-R. Chang, Hysteretic mutual phase-locking of perpendicular-to-plane polarizer spin-torque nano-oscillator pairs analyzed by a generalized pendulum-like model, *J. Appl. Phys.* **130**, 043904 (2021).
- [59] D. K. Lee, B. G. Park, and K. J. Lee, Antiferromagnetic oscillators driven by spin currents with arbitrary spin polarization directions, *Phys. Rev. Appl.* **11**, 054048 (2019).
- [60] C. X. Zheng, H. H. Chen, X. L. Zhang, Z. Zhang, and Y. Liu, Spin torque nano-oscillators with a perpendicular spin polarizer, *Chin. Phys. B* **28**, 037503 (2019).